Progress In Electromagnetics Research, Vol. 178, 49–62, 2023

High-Accuracy Rapid Identification and Classification of Mixed Bacteria Using Hyperspectral Transmission Microscopic Imaging and Machine Learning

He Zhu[1, 2], Jing Luo[1], Jiaqi Liao[1], and Sailing He[2, 1, *]

Abstract—In this paper, we developed a hyperspectral transmission microscopic imaging (HTMI) system for rapid detection of pathogenic bacteria, which can realize precise identification and classification of mixed pathogenic bacteria to a single-bacterium level. The system works in trans-illumination patterns and a self-developed dispersive hyperspectral imaging module is used as the detection setup, providing spectral images with high SNR, and showing excellent performances with spatial resolution of 2.19 µm and spectral resolutions less than 1 nm. Hyperspectral microscopic imaging of five types of bacteria in low concentration were performed. The merging spatial-spectral profiles of individual bacteria for each species were extracted and utilized for species identification, achieving high classification accuracy of 93.6% using a simple PCA-SVM method. Species identification experiments of the mixed bacterial samples were further carried out, and the results demonstrate the validity and capability of the system assisted with simple machine learning methods to be used as an effective and rapid diagnostic tool for elaborate identification of mixed bacterial pathogen samples, providing guidance for the use of correct antibiotics.

1. INTRODUCTION

Pathogenic bacterial infection is one of the challenging problems in the field of worldwide public health, which can be a significant threat to the physical health and life safety of the infected patient without prompt diagnosis and treatment [1–3]. Bacterial identification is a crucial process in the treatment of pathogenic infectious diseases, serving as the foundation for developing appropriate treatment protocols for patients, which is essential during clinical diagnosis [4, 5]. Currently, the conventional bacterial identification methods are mainly based on plate culture, which has the advantage of low-cost and reliable test results. However, it suffers from cumbersome and time-consuming steps including bacterial cultivation, purification, amplification and staining, resulting in missing the optimal time for diagnosis and treatment [6, 7]. The polymerase chain reaction (PCR) [8, 9] have strong specificity, but relies on expensive detection kits and thus is usually only used in emergency situations. Some identification approaches based on biosensors [10–12] are another research direction for rapid detection due to the lightweight and portable advantages. But they face the challenges of low specificity and cannot make effective judgments on complex electrical signals. How to achieve low-cost, high sensitivity, high automation, and real-time rapid pathogen identification is still an urgent problem to be solved in clinical medical diagnosis.

Hyperspectral imaging (HSI) combines two-dimensional (2D) images with spectra covering thousands of narrow wavelength bands, forming a three-dimensional hyperspectral cube of image-spectrum merging, with the advantages of non-invasive, non-destructive and label-free [13–15]. Some

Received 23 August 2023, Accepted 30 September 2023, Scheduled 1 October 2023
* Corresponding author: Sailing He (sailing@zju.edu.cn).
[1] Centre for Optical and Electromagnetic Research, National Engineering Research Center for Optical Instruments, Zhejiang Provincial Key Laboratory for Sensing Technologies, College of Optical Science and Engineering, Zhejiang University, Hangzhou 310058, China. [2] Taizhou Hospital, Zhejiang University, Taizhou, China.

miniaturized hyperspectral or multispectral systems have been proposed and used in the field of food safety assessment [16], disease diagnosis [17, 18], etc. For observation of microsamples and applications in microbiology, combing HSI and optical microscopy is a common and effective method to improve detection accuracy of samples at micron order or even nanoscale, and such hyperspectral microscopic imaging (HMI) has been as reported in the literatures with a wide range of applications, e.g., microalgae and fungi detection [19–21], tumor identification and growth stage assessment [22, 23], blood cells identification [24, 25], and so on.

Recently, a few experimental studies of pathologic bacteria diagnosis based on HMI have been reported [26–33]. Seo et al. have reported an identification method of *Staphylococcus* species using HMI and classical classification algorithms [26]. However, the use of an acousto-optic tunable filter (AOTF) for HMI greatly limits its spectral resolution to a few nanometers, which is insufficient for sophisticated analyses of the inherent biochemical materials. In 2018, the above research group have performed bacterial species classification based on the morphological characteristics in selected monochromatic spectral images selected from HMI [27], which demonstrates that the accuracy of classifying bacteria based only on morphological features of 2D images is limited (only 80.0%), and additional spectral information can be helpful for improving the quality of classification. Liu et al. have proposed a method to classify Gram-positive bacteria via HMI [28], but the characteristics spectral detection based on gram staining can be operationally tedious and lacking of timeliness. C. Tao et al. have presented an AI-assisted system for automagical identification of bacterial stains by combining HMI and self-developed Buffer Net [29]. In 2023, the authors have further designed an end-to-end deep learning network, called BI-Net, to extract species-dependent spectral fingerprints for pathologic classification [30]. In general, current researches of bacterial classification are mainly based on HMI techniques coupled with varying machine learning frameworks, e.g., 1D-CNN [31], Fusion-Net [32], and DenseNet [33], to achieve rapid identification.Some other computational models have also been utilized in the field of cancer identification [34, 35]. For identification of bacteria species, hyperspectral imaging is a cost-effective and efficient method, which eliminates the need for expensive detection kits and facilities, as well as time-consuming steps. It enables early detection at the cellular level. Limitations for such a method include the need for extensive dataset collection, accurate sample labeling, and comparing to the "golden truth" in order to improve the accuracy, sensitivity, and specificity of identification.

To further improve the classification accuracy, the development and optimization of the HMI system to realize finer spectral resolution and higher spatial resolution is essential, which is the key of the extraction and detection of robust species-dependent feature at single-cell level. In addition, previous studies primarily emphasize the recognition of individual bacterial species. However, the identification and classification of mixed bacteria in cases of multiple bacterial infection are critically important for accurate clinical diagnosis.

In this paper, we demonstrated a hyperspectral transmission microscopic imaging (HTMI) system for rapid identification and classification of mixed pathogenic bacteria to the single-cell level. Utilizing the self-developed dispersive hyperspectral imaging module, the system shows excellent performance, with spectral resolution less than 1 nm and spatial resolution of 2.19 μm, respectively (using 40× microscope objective magnification). We experimentally demonstrated the capabilities of the system by performing classification experiments at five types of bacteria. Hyperspectral cube of single bacterium was extracted from the hyperspectral microscopic images, and both the morphological differences and spectra were then used as the species-dependent features for bacterial classification. Using a PCA-SVM method, the average classification accuracy was found to be 93.6%. Furthermore, experiments of classifying mixed bacterial samples were conducted, which demonstrates the effectiveness and capability of the system as a rapid and reliable diagnostic tool for multiple bacterial infection, serving as guidance for correct antibiotic treatments.

The paper is organized as follows: Section 2 introduces the principle of operation of the HTMI system, as well as wavelength calibration and performance tests. In Section 3, classification experiments of five types of pathogenic bacteria, as well as identification experiment of mixed bacterial samples, were carried out based on the system combined with machine learning method. The paper ends with a summary and outlook in Section 4.

2. METHODS

2.1. System Setup and Calibration

Figure 1(a) shows detailed light path diagram of the system, with the physical photograph displayed in Fig. 1(b). The operating principle of the HTMI system is as follows. The lighting source is a high-power white LED with spectral range covering visible bands, which irradiates the sample in trans-illumination mode to provide sufficient luminous flux and improve the imaging (signal-noise-ratio) SNR. The transmission signal from the sample is then collected by a 40× magnification micro-objective (Olympus, Lumplflw), passing through a tube lens (Thorlabs, TTL200), and is divided into two paths by a beam splitter (BS). The combination of micro-objective and tube lens forms an infinity-corrected optical system, where the tube lens is used for achromatization and aberration correction, which can greatly improve the quality of microscopic imaging. One path of the light is reflected by the BS and imaged at the CMOS plane to form a microscope image. The imaging plane of the common microscope imaging module is conjugate with that of the hyperspectral imaging module, and thus the microscope image can be used a conjugated image for the convenience of observation and adjustment of focusing. Light from the other path of BS is converged and imaged at the plane where a 10 µm width slit is placed. One line region of the incident transmission light passing through the slit is then collimated by a collimator lens, and dispersed and expanded in the spectral range 450–800 nm by the prism-grating-prism (PGP), and then focused on the CMOS by an imaging lens. The spectrum of one line region can be obtained. By moving the specimen holder in the x or y direction through the motion stage, different line regions of the measurement sample can pass through the slit continuously and corresponding spectral information can be collected. After the push-broom scanning of the motion stage completed, the complete hyperspectral image can be obtained.

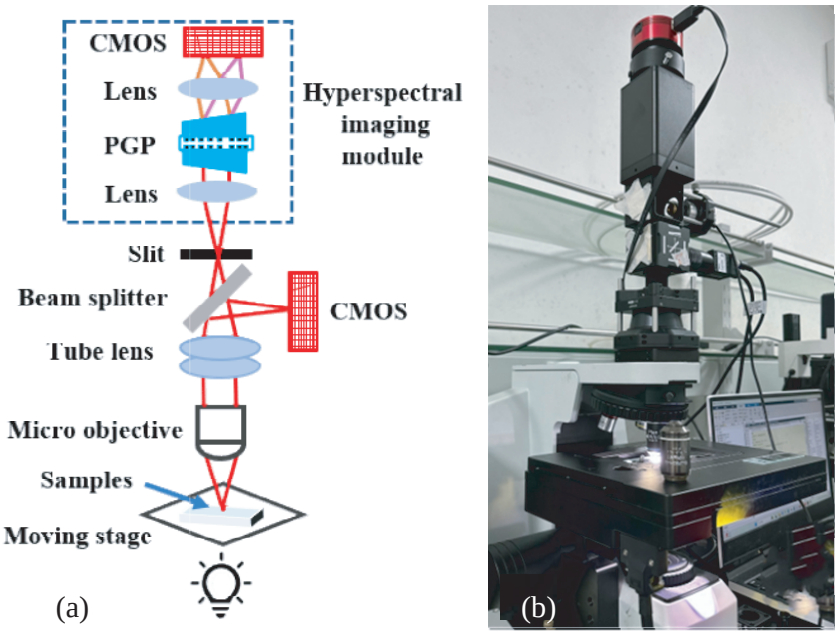

Figure 1. (a) Light path diagram and (b) physical photograph of the self-developed microscopic system.PGP: prism-grating-prism.

Spatial resolution has been characterized through performing hyperspectral imaging of a standard resolution test plane (LBTEK, USAF1951 RB-J). Fig. 2(a) shows the image result of the standard resolution test plane, with the enlargement pictures displaying the minimum line pairs. The minimum resolution patterns can be seen clearly, indicating the spatial resolution of the system is around 2.19 µm.

A Mercury Argon light is used as the calibration lighting source to illuminate the slit of the

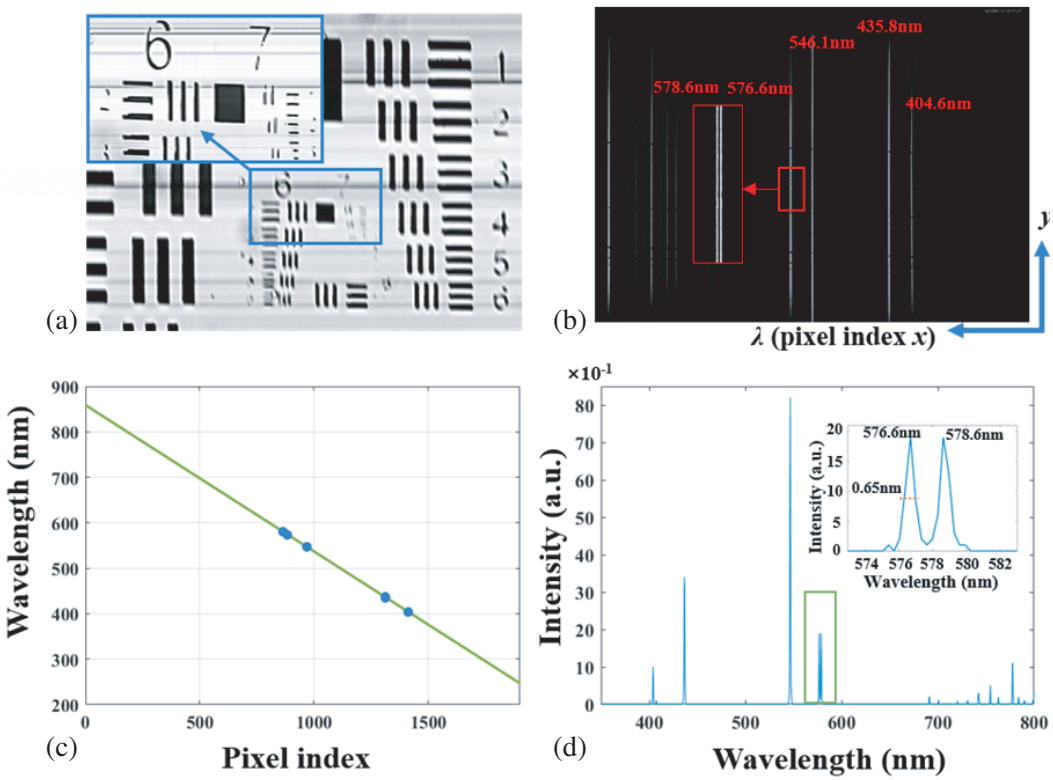

Figure 2. (a) Hyperspectral image of the standard resolution test board imaged by the system. (b) Spectral image of the Mercury Argon Calibration Source. (c) Relationship between the wavelength and pixel index as fitted by a second-order polynomial. (d) Spectral curve of the Mercury Argon Calibration Source measured by our systemforthe wavelength calibration.

hyperspectral imager, and the line light is then dispersed and expanded in the spectral range 400–800 nm by the PGP, and captured by the CMOS. The spectral image of the calibration lighting source is shown in Fig. 2(b). The x-axis represents the spectral axis since the spectrum expands along this axis, and the y-axis represents the spatial axis. The Mercury Argon lighting source emits multiple extremely narrow spectral lines at 404.6 nm, 435.8 nm, 546.1 nm, 576.6 nm, and 578.6 nm, corresponding to the five distinct lines seen in Fig. 2(b). The pixel indices for x corresponding to these wavelengths are 1410, 1311, 969, 876, and 870, respectively. The relationship between pixel index x and wavelength λ can be described by a polynomial function [36]:

$$\lambda = a_0 + a_1 x + a_2 x^2 \tag{1}$$

a_0, a_1, and a_2 are the calibration coefficients, which are calculated to be $[a_0, a_1, a_2] = [870.3, -0.3316, -1.7445e-06]$ using the polynomial least square method [36]. The polynomial result between the pixel index and wavelength value is shown in Fig. 2(c). Fig. 2(d) displays the spectral curve of the calibration source obtained by the hyperspectral imager following spectral calibration. The spectral resolution of the hyperspectral module depends on the maximum full width at half of the spectral peak, which is less than 1 nm. High spatial and spectral resolution of HMI enable high-precision morphological recognition and high-accuracy spectral differentiation of single micro bacteria.

2.2. Sample Preparation

Five types of food-borne bacterial pathogen, including *Staphylococcus aureus* (*S. aureus*), *Escherichia coliform* (*E. coli*), *Bacillus subtilis* (*B. subtilis*), *Pseudomonas aeruginosa* (*P. aeruginosa*), and *Salmonella* have been selected for the experiment. They were provided by Taizhou EnzeMedical

Center, Zhejiang. The pathogen involved in our experiments stemmed from common samples in clinical diagnosis, including urine, sputum, blood and tissue fluid.

All the bacteria were cultured on the blood plates in incubators for about 48 h to produce colonies. The pure isolated colony extracted from the culture dish were dissolved into sterile deionized (DI) water. And then, the bacterial solutions were centrifuged at 4500 rpm for 10 min to separate the pathogens. The bacterial pellets were re-suspended in 1.5 mL of DI water. For hyperspectral microscopic imaging, 10 µL of the suspension from each bacterial sample were dripped and spread at the center of a glass slide, covered with a 20 mm × 20 mm coverslip, for observation, imaging and analysis at the next step. Bacterial cultivations and isolation were carried out in a sterile condition to avoid sample pollution. And all bacterial suspensions for testing are freshly prepared and used only on the day of preparation. To minimize errors and ensure representative sampling, 50 sets of hyperspectral images were collected for each type of bacterial samples using 5 groups of specimens. In total, for species classification experiments, 250 (50 × 5) microscopic hyperspectral images for five different types of bacteria were obtained and further analysis.

3. RESULTS AND DISCUSSION

In this section, we detailed a range of bacteria species detection and classification experiments using our self-developed HTMI system. Hyperspectral imaging results of five types of bacteria and the classification performance of bacterial species using PCA-SVM computational methods have been displayed. We furthermore demonstrated the validity of the system to classify bacteria species in low concentrations, as well as the capability of species identification of mixed bacterial samples. All the experiments were carried out in the microbiology labat Taizhou Hospital for preparing and controlling pathogenic bacteria.

3.1. Hyperspectral Imaging of Five Species of Bacteria

After sample preparation, the glass slide covered with bacterial samples was placed at the motion stage and adjusted to be in focus for clear imaging. And then, the glass slide was moved at the intervals of 1 µm with the horizontal displacement of the motion stage, and corresponding spectral data of the line region was collected by the hyperspectral imaging module until the entire imaging region is scanned. A total number of 1000 hyperspectral images from various line regions were collected in succession and combined into a complete 3D hyperspectral cube following push-broom scanning. The total scanning time for one hyperspectral imaging is about 30 s, which can be further reduced by increasing light source intensity, and using a CMOS sensor with higher detection sensitivity and efficiency, etc. Fig. 3 displays the hyperspectral images of the five types of bacteria, *E. coli*, *S. aureus*, *B. subtilis*, *Salmonella*, and *P. aeruginosa*, from left to right respectively. The concentration of the bacteria is around 10^8/mL. Here,

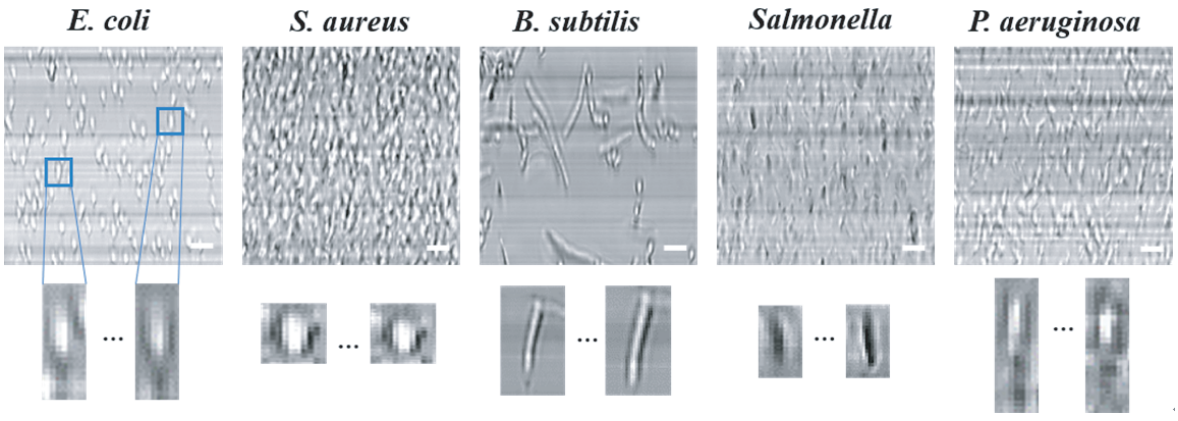

Figure 3. Hyperspectral images of 5 different types of bacteria: *E. coli*, *S. aureus*, *B. subtilis*, *Salmonella*, and *P. aeruginosa*. (Scale bar: 2 µm).

we utilized a 40× magnification microscope objective to observe the bacteria samples. The enlarged pictures in Fig. 3 shows the morphological profile of single bacterium. The *S. aureus* circular in shape, while the *E. coli*, *B. subtilis*, and *P. aeruginosa* are rod-shaped. The morphological features of different bacteria species can be clearly seen and distinguished through the hyperspectral images, indicating the high spatial resolution and excellent imaging performance of the system. By replacing the objective with a higher magnification one, the difference in morphology and size characteristics of various bacteria species can be magnified, though the demand of luminous flux will be largely increased as well.

Precise spectra and morphological features of bacteria can be automatically derived from the hyperspectral images using regions of interest (ROI) separation. Taking the spectral image of *E. coli* as an example, the spatial hyperspectral image of *E. coli* is transferred to a gray image, as shown in Fig. 4(a). In our work, we identified the ROI by segmenting the single bacterium from the background using a edge detection, erosion and dilation based on pixel gray value differences. The bacteria appear as regions with relatively high gray value at the central area and low gray value at the edge, while the background presents as the one with moderate gray value. An image filter is utilized to reduce noise. Fig. 4(b) displays the segmented binary image, serving as the image mask template. After imaging masking, each ROI was occupied by one individual bacterium and can be successfully extracted, containing both spectral data and shape features. The transmission spectrum of one single bacterium (in the ROI) can be calculated to be:

$$\overline{T(\lambda)} = \frac{1}{Num} \sum_{x,y} H(x, y, \lambda), (x, y) \in ROI \tag{2}$$

where the Num represents the number of pixels in a single bacterial region (one ROI), and $H(x, y, z)$ is the spectral data of a bacterial pixel at coordinate (x, y). The transmission spectra for a single bacterium can be obtained from Eq. (2). Fig. 4(c) shows the spectral curves for about 20 individual bacteria extracted from Fig. 4(b), from which one sees that the transmission spectra for the same type of bacteria are quite similar.

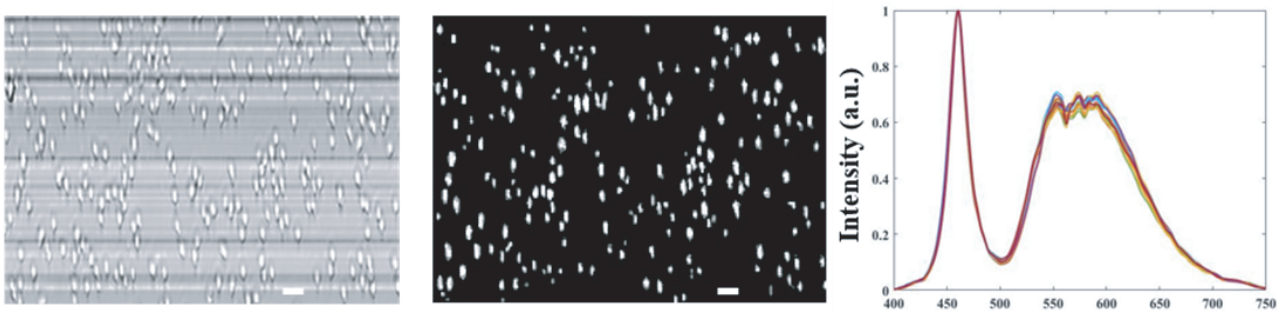

Figure 4. (a) Gray spatial hyperspectral images of *E. coli*. (b) The binary image mask template. (c) The spectra extracted from (b) for about 20 bacteria, each curve gives the transmission spectra for an individual bacterium. (Scale bar: 2 μm).

The transmission intensity spectra of the five types of bacteria are shown in Fig. 5(a), with spectral range from 400 nm to 750 nm. Although material composition of bacteria is roughly the same, including peptidoglycans, lipopolysaccharides, lipoproteins, etc., the differences in material content and biological structure form unique spectral characteristics of specific type of bacteria species. The substances produced by the interaction between the bacterial colonies and culture materials can also affect spectral characteristics. For example, the *P. aeruginosa* produces pyocyanin on the blood plate, presenting blue-green color. Figs. 5(b)–(f) show the normalized transmissivity spectra of five bacteria species at the valid wavelength range of 500 nm–650 nm, respectively. These spectra are derived by dividing the intensity spectra of the bacteria by the spectrum of lighting source, which can reduce the influence of lighting source on bacterial spectra. Each expanded shadow indicates the deviation of different individual bacteria of the specific type. The magnitude of the rise and decline varied among spectral curves of

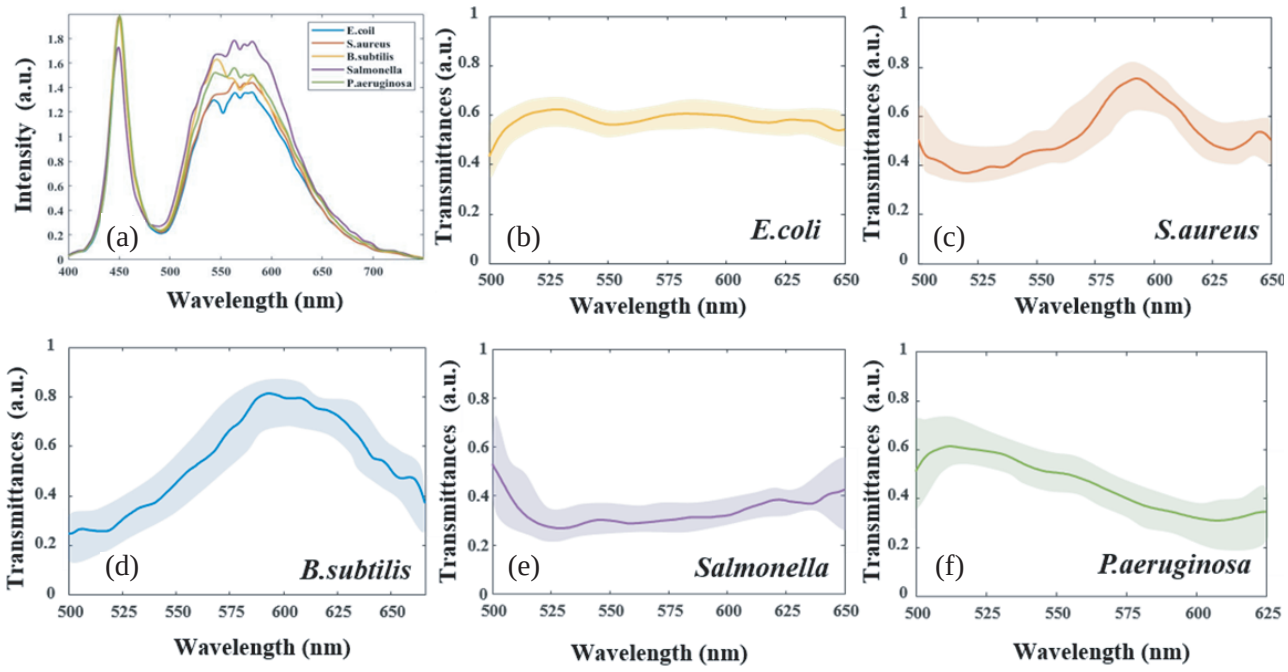

Figure 5. Verification of spectral characteristics of five different types of bacteria. (a) Transmission intensity spectral curves of the five types of bacteria. Normalized transmissivity spectral curves with the influence of the light source eliminated: (b) *E. coli*, (c) *S. aureus*, (d) *B. subtilis*, (e) *Salmonella*, and (f) *P. aeruginosa*.

different types of bacteria. The spectra curves of *P. aeruginosa* are relatively smooth, with transmission bands concentrated between 520 nm and 560 nm, indicating a dark green color characteristic. The spectra of *S. aureus* have a transmission peak located around 580 nm, corresponding to a yellow color.

3.2. Classification of Bacteria Species Based on PCA-SVM Method

The spectral differences of bacteria species can serve as a basis of pathogens identification and classification. To verify the validity of hyperspectral images in species classification, we compared the classification performance using two data types as follows: 1) traditional gray images, containing morphological information of the bacteria, e.g., extent area, perimeter, axis length and aspect ratio; 2) hyperspectral images with both spatial information and spectral characteristics. The two types of datasets were used as input for a machine learning algorithm, separately.

Single gray bacterial imaging data was employed for bacterial classification. To reduce data redundancy and maximize data variance, principal component analysis (PCA) approach is used to transform the original imaging date into a smaller set of uncorrelated components, known as principal components (PCs) [37, 38]. These components are ranked based on their variance, with the first component capturing the most variance. After dimension reduction, support vector machine (SVM) [39–41] is applied on the transformed data to classify and predict new instances. It finds an optimal hyperplane that separates different classes in the reduced feature space. We employed a linear SVM algorithm to classify the five categories of samples. The separation regions were determined using the first two principal components (PC1 and PC2), as illustrated in Fig. 6(a). Several metrics, including accuracy, sensitivity, and specificity are introduced to evaluate the performance of the classification algorithm [42, 43]. Predictive accuracy measures the overall correctness of a classifier by calculating the ratio of correctly predicted instances to the total number of instances. Sensitivity, or True Positive (TP) Rate, is calculated by dividing TP by the sum of TP and false negatives (FN). Specificity is determined by dividing TN by the sum of TN and false positives (FP). Precision can be used to evaluate the reliability of the classifier in correctly identifying positive samples, which is calculated by dividing the

number of TP results by the sum of TP and FP. The calculation expressions for these four metrics are expressed as follows.

$$Accuracy = \frac{TP + TN}{TP + FP + FN + TN} \tag{3a}$$

$$Sensitivity = \frac{TP}{TP + FN} \tag{3b}$$

$$Specificity = \frac{TN}{TN + FP} \tag{3c}$$

$$Precision = \frac{TP}{FP + TP} \tag{3d}$$

The predictive accuracy provides an overall view of the classifier's performance, while sensitivity and specificity focus on different aspects of classification performance in terms of positive and negative instances. The classification results based on the binary bacterial imaging data (using are presented in Fig. 6(b). The results in the confusion matrix indicated that 80% accuracy was achieved. Specifically,classification accuracies are 88.0%, 82%, 92.1%, 8.0%, and 54.0% for *E. coli*, *S. aureus*, *B. subtilis*, *Salmonella*, and *P. aeruginosa*, respectively. Little improvement can be made by using more principal components. The sensitivity and specificity to distinguish one species from other four species were calculated to be 74.6% and 85.8%, respectively. The precision to distinguish one species (*E. coli*, *S. aureus*, *B. subtilis*, *Salmonella*, and *P. aeruginosa*) from others were 83.0%, 89.1%, 67.8%, 100%, 61.4%. The receiver operating characteristic (ROC) curves are plotted in Fig. 6(c), and the area under curve (AUC) for each classification scenario were 0.97, 0.97, 0.93, 1.00, and 0.85, respectively.

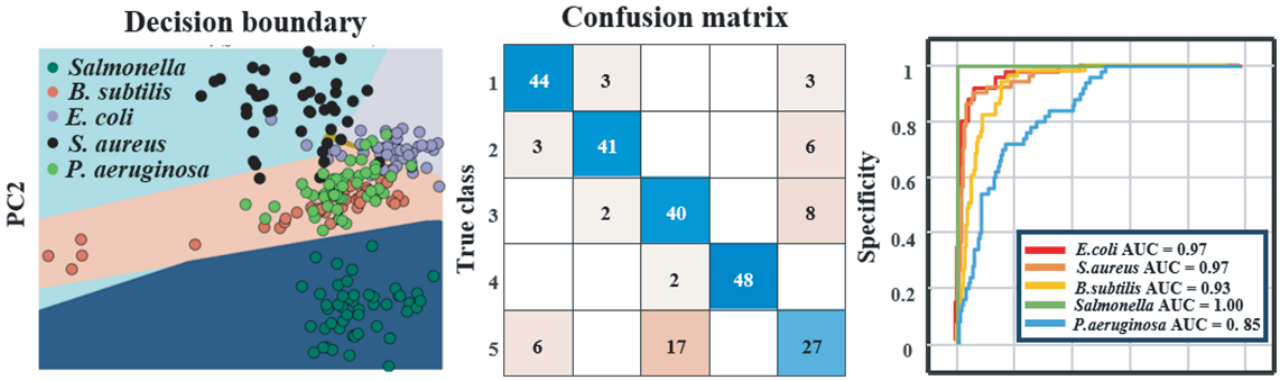

Figure 6. (a) Segmentation region of the gray images based on PC1 and PC2. (b) The confusion matrix visualizes the accuracy obtained from PCA-SVM over 250 gray images of individual bacteria. 1: *E. coli*; 2: *S. aureus*; 3: *B. subtilis*; 4: *Salmonella*; 5: *P. aeruginosa*. (c) The ROC curves corresponding to the SVM classifier in (a).

We also studied the bacterial classification performance using single hyperspectral bacterial imaging data, which encoded both spatial characteristics and spectral features. After PCA processing, both the two-dimensional image information and spectra are transformed into PCs. The first two PCs of each dataset that corresponding to the same single bacterium are used as input for linear SVM classifier. Due to the high dimensionality of the hyperspectral imaging dataset, visualizing the SVM segmentation regions on a 2D plane can be challenging, and is thus omitted in Fig. 7. Fig. 7(a) shows the confusion matrix and the average accuracy, sensitivity and specificity were calculated to be 93.6%, 93.6% and 98.4%, respectively. The precision to distinguish one species (*E. coli*, *S. aureus*, *B. subtilis*, *Salmonella*, and *P. aeruginosa*) from others were 86.5%, 87.8%, 100%, 100%, 93.9%. The ROC curves are shown in Fig. 7(b). In the segmentation results illustrated in Fig. 6(a), which using grey imaging data as input, we see that the *E. coli*, *B. subtilis*, and *P. aeruginosa* can be hardly distinguished, as all three are

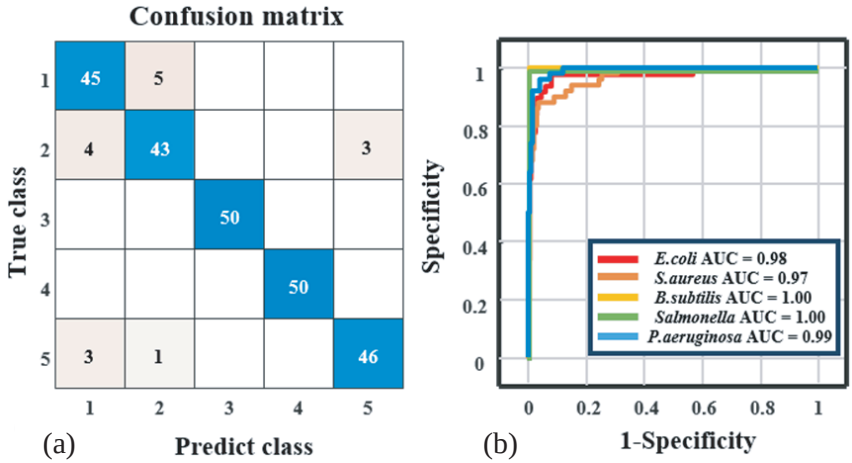

Figure 7. (a) The confusion matrix visualizes the classification accuracy obtained from PCA-SVM over 250 hyperspectral images of individual bacteria. 1: *E. coli*; 2: *S. aureus*; 3: *B. subtilis*; 4: *Salmonella*; 5: *P. aeruginosa*. (b) The ROC curves corresponding to the SVM classifier.

rod-shaped with small morphological differences. Spectral data provides another dimension of feature information relative to the biochemistry of the species, which can help greatly increase the accuracy of identification and classification.

3.3. Bacteria Species Identification of Low Concentration Samples and Mixed Solution

Since the identification of single bacterium at nanoscale can be achieved using precise image-spectrum merging information, as discussed in Section 3.2, we also considered the classification performance of bacteria colonies/solutions in low concentration, as well as the mixed samples. Classification experiments of low concentration bacteria were carried out. Dilute the bacterial samples from Section 3.2 by a factor of 10, and apply 10 µL of the diluted suspension for each species onto a glass slide for detection. Fig. 8 shows the hyperspectral images of the diluted suspension of *E. coli*, *S. aureus*, *B. subtilis*, *Salmonella*, and *P. aeruginosa*, where the number of bacteria has significantly decreased. We collected a total of 250 hyperspectral images (50 sets per bacterial species) for species recognition and further analysis. The classification results are presented in Fig. 9(a), where the results of the confusion matrix indicating that the average accuracy calculated to be 9.4%, respectively. The ROC curves, with AUC of 0.97, 0.98, 0.99, 1.00, and 0.97, are plotted in Fig. 9(b). For bacteria colonies/solutions in low concentration, light absorption of the biochemical substances is low, resulting in poor sensitivity for detection and identification of single bacterium. However, benefiting from the high spectral-spatial resolution of the self-developed hyperspectral microscopic system, high accuracy of above 90% can still be maintained in

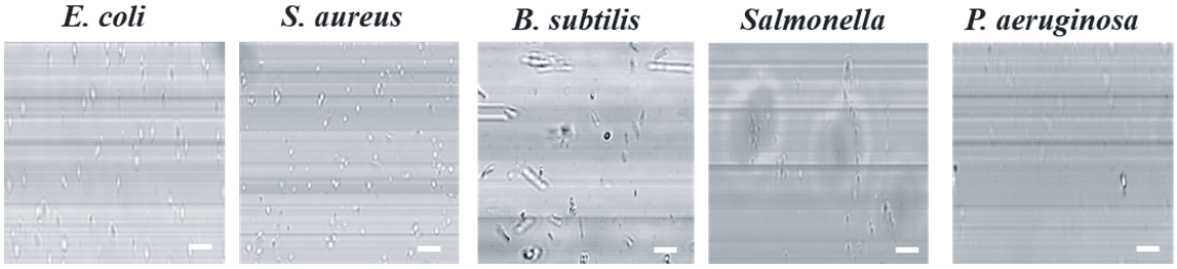

Figure 8. Hyperspectral images of diluted suspensions of *E. coli*, *S. aureus*, *B. subtilis*, *Salmonella*, and *P. aeruginosa*. (Scale bar: 2 µm).

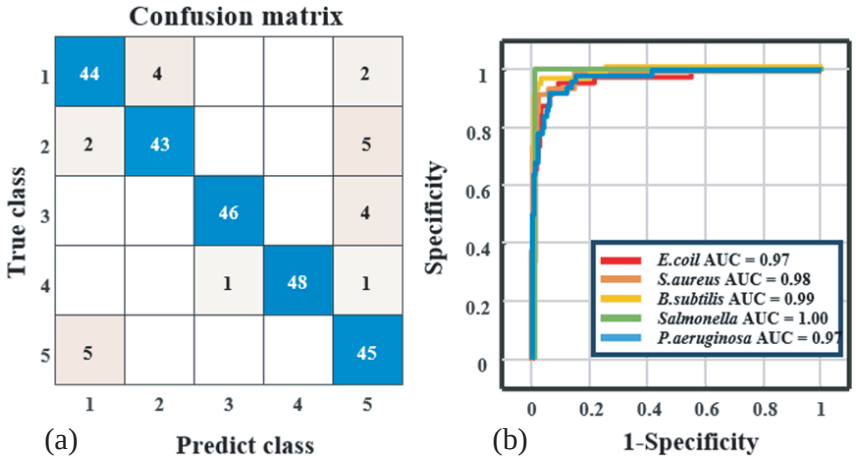

Figure 9. (a) The confusion matrix visualizes the classification accuracy achieved by PCA-SVM over 250 hyperspectral images of individual bacteria after diluting. 1: *E. coli*; 2: *S. aureus*; 3: *B. subtilis*; 4: *Salmonella*; 5: *P. aeruginosa*. (b) The ROC curves corresponding to the SVM classifiers.

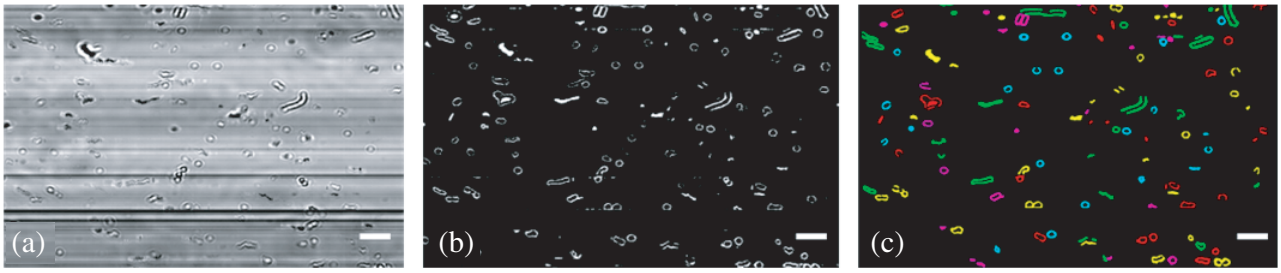

Figure 10. Species identification of mixed bacterial samples. (a) Gray hyperspectral image of the mixed bacteria at the broad visible bands. (b) The image after the edge detection. (c) The classification results (on the image mask) by the PCA-SVM method. *E. coli*, *S. aureus*, *B. subtilis*, *Salmonella*, and *P. aeruginosa* were rendered in the different colors of red, turquoise, green, magenta, and yellow respectively. (Scale bar: 5 μm).

low concentration bacterial detection, which has great potential application values in clinical testing.

Furthermore, we have carried out species identification of mixed bacteria in a similar way. Five diluted suspensions of different bacterial species were combined in equal amounts and placed in a test tube, which was then shaken and dripped onto a glass slide for imaging. Fig. 10(a) displays the transmission hyperspectral image of the mixed bacteria samples, which makes it difficult to distinguish specific species. To extract single bacterial area from the image background, the imaging process methods including edge detection, erosion and dilation were employed, resulting in the binary image shown in Fig. 10(b). Both morphological and hyperspectral features of all bacteria can be extracted and utilized for the classification labels of the PCA-SVM algorithm, with the identification results depicted in Fig. 10(c). Based on the recognition outcomes, the five mixed bacteria species of *E. coli*, *S. aureus*, *B. subtilis*, *Salmonella*, and *P. aeruginosa* were represented by the colors of red, turquoise, green, magenta, and yellow, respectively. The concentration ratio of the five bacteria after PCA-SVM classification is roughly equal, consistent with the results of previous equal mixing. Such an experiment verifies the effectiveness of our rapid method in extraction, recognition, and classification of multiple mixed bacteria, and has potential applications in bacterial infection analysis, providing diagnostic basis for the use of correct antibiotics.

4. SUMMARY AND OUTLOOK

In this paper, we have presented a hyperspectral transmission microscopic (HTMI) system for elaborate hyperspectral imaging of pathogenic bacteria at single-cell level, which can realize precise identification and classification of single and mixed bacterial samples using simple PCA-SVM method. The system works in trans-illumination mode and utilizes a high-power LED as the light source, thereby increasing the luminous flux and improving the SNR of the spectral images. The self-developed dispersive hyperspectral module serves as the spectral detection setup, exhibiting outstanding microscopy performance with spatial resolution of 2.19 µm and spectral resolution less than 1 nm. In the experiments, we have first performed hyperspectral microscopic imaging of five bacterial species in low concentration. The single-cell hypercubes containing abundant morphological features and spectral information were then extracted from the hyperspectral images, and used for species identification. With the PCA-SVM method, we achieved a classification accuracy of 93.6% in distinguish one species from four others. Additionally, we conducted species identification experiments with mixed bacterial samples, and the results showcase the system's practicality in clinical multiple bacterial infection diagnosis and correct antibiotic treatments. The HTMI system provides a feasible and effective method for high-accuracy, real-time detection and identification of single and mixed bacterial pathogen samples, which is of great significant of clinical microbial confirmation and diagnosis.

In terms of further improvements, the sampling datasets can be expanded, and the classifying models can be updated, allowing for identification of diverse bacterial species. Fluorescence hyperspectral detection can be employed into the TMHI system to provide more specific information relative to bacterial species, which can help improve the classification accuracy. The system can be transformed from push-broom scanning to staring scanning mode by introducing a galvanometer, which can reduce the impact of sample movement on image quality, as well as further greatly improve imaging speed.

ACKNOWLEDGMENT

This work is partially supported by the "Pioneer" and "Leading Goose" R&D Program of Zhejiang (No. 2023C03083 and 2023C03135), the National Key Research and Development Program of China (No. 2022YFC2010000 and 2022YFC3601000) and the National Natural Science Foundation of China (Nos. 11621101). The authors are grateful to Dr. Julian Evans and Xiaer Zhou of Zhejiang University and Jiao Qian of Taizhou Hospital for valuable discussions.

DATA AVAILABILITY

Data underlying the results presented in this paper are not publicly available at this time but may be obtained from the authors upon reasonable request.

DISCLOSURES

The authors declare no conflicts of interest.

REFERENCES

1. Ward, J. L., P. S. Azzopardi, K. L. Francis, et al., "Global, regional, and national mortality among young people aged 10–24 years, 1950–2019: A systematic analysis for the Global Burden of Disease Study 2019," *Lancet*, Vol. 398, 1593–1618, 2021.
2. Beutlich, J., J. A. Hammerl, B. Appel, et al., "Characterization of illegal food items and identification of foodborne pathogens brought into the European Union via two major German airports," *International Journal of Food Microbiology*, Vol. 209, 13–19, 2015.

3. Galanis, E., J. Parmley, W. N. De, et al., "Integrated surveillance of Salmonella along the food chain using existing data and resources in British Columbia, Canada," *Food Research International*, Vol. 45, No. 2, 795–801, 2012.
4. Kumar, A., P. Ellis, Y. Arabi, et al., "Initiation of inappropriate antimicrobial therapy results in a fivefold reduction of survival in human septic shock," *Chest*, Vol. 136, No. 5, 1237–1248, 2009.
5. Gan, Y., C. Li, X. Peng, et al., "Fight bacteria with bacteria: Bacterial membrane vesicles as vaccines and delivery nanocarriers against bacterial infections," *Nanomedicine-Nanotechnology Biology and Medicine*, Vol. 35, 102398, 2021.
6. Fratamico, P. M., "Comparison of culture, polymerase chain reaction (PCR), TaqMan Salmonella, and Transia Card Salmonella assays for detection of Salmonella spp. in naturally-contaminated ground chicken, ground turkey, and ground beef," *Molecular and Cellular Probes*, Vol. 17, No. 5, 215–221, 2003.
7. Bolton, F. J., E. Fritz, S. Poynton, et al., "Rapid enzyme-linked immunoassay for detection of salmonella in food and feed products: Performance testing program," *Journal of Aoac International*, Vol. 83, No. 2, 299–303, 2000.
8. Compton, J., "Nucleic acid sequence-based amplification," *Nature*, Vol. 350, No. 6313, 91–2, 1991.
9. Engelmann, I., E. K. Alidjinou, J. Ogiez, et al., "Preanalytical issues and cycle threshold values in SARS-CoV-2 real-time RT-PCR testing: Should test results include these," *Acs Omega*, Vol. 6, No. 10, 6528–6536, 2021.
10. Pal, S., W. Ying, E. C. Alocija, et al., "Sensitivity and specificity performance of a direct-charge transfer biosensor for detecting Bacillus cereus in selected food matrices," *Biosystems Engineering*, Vol. 99, No. 4, 461–468, 2008.
11. Esteban-Fernandez De Avila, B., M. Pedrero, S. Campuzano, et al., "Sensitive and rapid amperometricmagnetoimmunosensor for the determination of Staphylococcus aureus," *Analytical and Bioanalytical Chemistry*, Vol. 403, No. 4, 917–925, 2012.
12. Munoz-Berbel, X., N. Vigues, A. T. A. Jenkins, et al., "Impedimetric approach for quantifying low bacteria concentrations based on the changes produced in the electrode-solution interface during the pre-attachment stage," *Biosensors & Bioelectronics*, Vol. 23, No. 10, 1540–1546, 2008.
13. Luo, J., Z. Lin, X. Xing, E. Forsberg, C. Wu, X. Zhu, T. Guo, G. Wang, B. Bian, D. Wu, and S. He, "Portable 4D snapshot hyperspectral imager for fastspectral and surface morphology measurements (Invited Paper)," *Progress In Electromagnetics Research*, Vol. 173, 25–36, 2022.
14. Guo, T., Z. Lin, X. Xu, Z. Zhang, X. Chen, N. He, G. Wang, Y. Jin, J. Evans, and S. He, "Broad-tuning, dichroic metagrating fabry-perot filter based on liquid crystal for spectral imaging," *Progress In Electromagnetics Research*, Vol. 177, 43–51, 2023.
15. Pawlowski, M. E., J. G. Dwight, N. Thuc Uyen, et al., "High performance image mapping spectrometer (IMS) for snapshot hyperspectral imaging applications," *Optics Express*, Vol. 27, No. 2, 1597–1612, 2019.
16. Wang, T., F. Shen, H. Deng, et al., "Smartphone imaging spectrometer for egg/meat freshness monitoring," *Analytical Methods*, Vol. 14, No. 5, 508–517, 2022.
17. Shen, F., H. Deng, L. Yu, et al., "Open-source mobile multispectral imaging system and its applications in biological sample sensing," *Spectrochimica Acta, Part A: Molecular and Biomolecular Spectroscopy*, Vol. 280, 121504, 2022.
18. Li, Y., F. Shen, and L. Hu, "A stare-down video-rate high-throughput hyperspectral imaging system and its applications in biological sample sensing," *IEEE Sensors Journal*, 2023, doi: 10.1109/JSEN.2023.3308394.
19. Xu, Z., Y. Jiang, J. Ji, et al., "Classification, identification, and growth stage estimation of microalgae based on transmission hyperspectral microscopic imaging and machine learning," *Optics Express*, Vol. 28, No. 21, 30686–30700, 2020.
20. Lin, S., X. Bi, S. Zhu, et al., "Dual-type hyperspectral microscopic imaging for the identification and analysis of intestinal fungi," *Biomedical Optics Express*, Vol. 9, No. 9, 4496–4508, 2018.

21. Luo, J., H. Zhang, E. Forsberg, et al., "Confocal hyperspectral microscopic imager for the detection and classification of individual microalgae," *Optics Express*, Vol. 29, No. 23, 37281–37301, 2021.
22. Maktabi, M., Y. Wichmann, H. Koehler, et al., "Tumor cell identification and classification in esophageal adenocarcinoma specimens by hyperspectral imaging," *Scientific Reports*, Vol. 12, No. 1, 4508, 2022.
23. Zhu, S., K. Su, Y. Liu, et al., "Identification of cancerous gastric cells based on common features extracted from hyperspectral microscopic images," *Biomedical Optics Express*, Vol. 6, No. 4, 1135–1145, 2015.
24. Duan, Y., J. Wang, M. Hu, et al., "Leukocyte classification based on spatial and spectral features of microscopic hyperspectral images," *Optics & Laser Technology*, Vol. 112, 530–538, 2019.
25. Wang, Q., J. Wang, M. Zhou, et al., "Spectral-spatial feature-based neural network method for acute lymphoblastic leukemia cell identification via microscopic hyperspectral imaging technology," *Biomedical Optics Express*, Vol. 8, 3017–3028, 2017.
26. Seo, Y., B. Park, A. Hinton, Jr., et al., "Identification of Staphylococcus species with hyperspectral microscope imaging and classification algorithms," *Journal of Food Measurement and Characterization*, Vol. 10, No. 2, 253–263, 2016.
27. Seo, Y., B. Park, S. C. Yoon, et al., "Morphological image analysis for foodborne bacteria classification," *Transactions of the Asabe*, Vol. 61, No. 1, 5–13, 2018.
28. Liu, K., Z. Ke, P. Chen, et al., "Classification of two species of Gram-positive bacteria through hyperspectral microscopy coupled with machine learning," *Biomedical Optics Express*, Vol. 12, No. 12, 7906–7916, 2021.
29. Tao, C., J. Du, Y. Tang, J. Wang, et al., "A deep-learning based system for rapid genus identification of pathogens under hyperspectral microscopic images," *Cells*, Vol. 11, No. 14, 2237, 2022.
30. Tao, C., J. Du, J. Wang, et al., "Rapid identification of infectious pathogens at the single-cell level via combining hyperspectral microscopic images and deep learning," *Cells*, Vol. 12, No. 3, 379, 2023.
31. Kang, R., B. Park, M. Eady, et al., "Classification of foodborne bacteria using hyperspectral microscope imaging technology coupled with convolutional neural networks," *Applied Microbiology and Biotechnology*, Vol. 104, No. 7, 3157–3166, 2020.
32. Kang, R., B. Park, M. Eady, et al., "Single-cell classification of foodborne pathogens using hyperspectral microscope imaging coupled with deep learning frameworks," *Sensors and Actuators B-Chemical*, Vol. 309, 127789, 2020.
33. Huang, G., Z. Liu, L. Van Der Maaten, et al., "Densely connected convolutional networks," *Proceedings of the IEEE Conference on Computer Vision and Pattern Recognition*, 4700–4708, Honolulu, HI, USA, July 21–26, 2017.
34. Farooq, S., M. Del-Valle, M. O. dos Santos, et al., "Rapid identification of breast cancer subtypes using micro-FTIR and machine learning methods," *Applied Optics*, Vol. 62, No. 8, C80–C87, 2023.
35. Farooq, S., A. Caramel-Juvino, and M. Del-Valle, "Superior machine learning method for breast cancer cell lines identification," *2022 SBFoton International Optics and Photonics Conference (SBFoton IOPC)*, 1–3, 2022.
36. Cho, J. H., P. J. Gemperline, and D. Walker, "Wavelength calibration method for a CCD detector and multichannel fiber-optic probes," *Appl. Spectrosc.*, Vol. 49, No. 12, 1841–1845, 1995.
37. Wold, S., K. Esbensen, and P. Geladi, "Principal component analysis," *Chemom. Intell. Lab. Syst.*, Vol. 2, Nos. 1–3, 37–52, 1987.
38. Bro, R. and A. K. Smilde, "Principal component analysis," *Analytical Methods*, Vol. 6, No. 9, 2812–2831, 2014.
39. Melgani, F. and L. Bruzzone, "Classification of hyperspectral remote sensing images with support vector machines," *IEEE Transactions on Geoscience and Remote Sensing*, Vol. 42, No. 8, 1778–1790, 2004.

40. Moughal, T. A., "Hyperspectral image classification using support vector machine," *Journal of Physics Conference*, Vol. 439, 012042, 2013.
41. Yang, W. and H. Song, "Spectral-spatial classification of hyperspectral image based on support vector machine," *International Journal of Information Technology and Web Engineering*, Vol. 16, No. 1, 56–74, 2021.
42. De Oliveira, M. A. S., M. Campbell, A. M. Afify, et al., "Hyperspectral Raman microscopy can accurately differentiate single cells of different human thyroid nodules," *Biomedical Optics Express*, Vol. 10, No. 9, 4411–4421, 2019.
43. Luo, J., H. Lin, A. Yang, et al., "Pulse fluorescence LIDAR system for identification and low concentration measurements of Phaeocystisglobosa cells and colonies," *Optik*, Vol. 270, 170003, 2022.